Title

Strain-Induced Quantum Phase Transitions in Magic-Angle Graphene

Journal

Physical Review Letters, 127(2)

ISSN

0031-9007

Authors

Parker, Daniel E

Soejima, Tomohiro

□□□□

et al.

Publication Date

2021-07-09

DOI

10.1103/physrevlett.127.027601

Peer reviewed

Strain-Induced Quantum Phase Transitions in Magic-Angle Graphene

Daniel E. Parker,[1,2] Tomohiro Soejima (副島智大),[2] Johannes Hauschild,[2] Michael P. Zaletel,[2,3] and Nick Bultinck[2,4]
[1]*Department of Physics, Harvard University, Cambridge, Massachusetts 02138, USA*
[2]*Department of Physics, University of California, Berkeley, California 94720, USA*
[3]*Materials Sciences Division, Lawrence Berkeley National Laboratory, Berkeley, California 94720, USA*
[4]*Department of Physics, Ghent University, 9000 Ghent, Belgium*

We investigate the effect of uniaxial heterostrain on the interacting phase diagram of magic-angle twisted bilayer graphene. Using both self-consistent Hartree-Fock and density-matrix renormalization group calculations, we find that small strain values ($\epsilon \sim 0.1\%$–0.2%) drive a zero-temperature phase transition between the symmetry-broken "Kramers intervalley-coherent" insulator and a nematic semimetal. The critical strain lies within the range of experimentally observed strain values, and we therefore predict that strain is at least partly responsible for the sample-dependent experimental observations.

Experiments on different twisted bilayer graphene (TBG) devices, all close to the first magic angle, have produced a broad variety of different low-temperature phase diagrams. For example, at the charge neutrality point (CNP), both semimetallic [1–6] and insulating [7–11] states have been observed. The insulating devices are thought to be divided into two groups. In the first group [7,8], one of the graphene sheets is almost perfectly aligned with the hexagonal boron-nitride substrate, which breaks the two-fold rotation symmetry and therefore generates mass terms for the Dirac cones [12–17] in the single-particle continuum model of TBG [18–20]. In the second group of devices [9,11], those without substrate alignment, the Coulomb interaction is believed to be responsible for the insulating behavior. Both analytical and numerical studies [21,22] of pristine TBG at the CNP indeed find an insulating ground state due to spontaneous "Kramers intervalley-coherent" (K-IVC) order [22]. The K-IVC state is thus a promising candidate for the CNP insulators in Ref. [9] as well as the $|\nu| = 2$ insulators in general, but it cannot explain the semimetals observed in Refs. [1,3–6]. Moreover, self-consistent Hartree-Fock (SCHF) predicts a K-IVC gap of $\sim$20 meV [22], while experiments measure a global transport gap of only $\sim$1 meV [9].

Thus, an important question is this: what weakens the insulators in some experimental devices and destroys them in others? Twist-angle disorder is expected to be at least partly responsible for this phenomenon [23–26]. Another possible culprit is the presence of strain in the graphene sheets. Uniaxial heterostrain is characterized by a parameter ϵ, which scanning tunneling spectroscopy experiments have found to be in the range $\epsilon = 0.1\%$–0.7% [27–29]. Although these values seem small at face value, strain contributes to the Hamiltonian as a perturbation of order $\epsilon\hbar v_F/a$, which is $\sim$20 meV for $\epsilon = 0.5\%$—precisely the energy scale at issue. Further evidence for the importance of strain comes from symmetry considerations. In the absence of strain, models at even-integer filling show that, although the ground state has K-IVC order, there is a close competitor whose energy is only slightly higher: a nematic semimetal [22,28,30–32]. As elucidated in Ref. [30], the semimetal has two Dirac points close to, but not at, the mini-BZ Γ point, spontaneously breaking the threefold rotational symmetry C_{3z}. The shear part of uniaxial strain breaks the C_{3z} symmetry, and thus one expects on general grounds that strain will lower the energy of the nematic semimetal relative to the rotationally invariant insulating states. However, despite this expectation, Refs. [22,30] found that if strain is modeled using the phenomenological method of Ref. [33], it cannot stabilize the semimetal.

This Letter provides a careful treatment of the effects of strain on the correlated insulators using a more realistic model for strained TBG [34]. We find that physical strain values can drive a zero-temperature phase transition from the K-IVC insulator to a semimetal at even-integer fillings. Our results at charge neutrality are obtained using SCHF, and our results at $\nu = -2$ (ν is the number of electrons per moiré unit cell relative to charge neutrality) using both the density-matrix renormalization group (DMRG) algorithm and SCHF. Our DMRG considers both valley degrees of freedom, which is essential for correctly identifying the even-integer insulators. Similar to earlier works on single-valley models [31,32], we find that DMRG and SCHF agree remarkably well. In particular, DMRG confirms the presence of K-IVC order at $\nu = -2$ in the absence of strain.

Continuum model with strain.—To add uniaxial strain to the Bistritzer-MacDonald (BM) continuum Hamiltonian [18–20], we follow Ref. [34]. Uniaxial strain is characterized by the following symmetric matrix:

$$\mathsf{S} = \begin{pmatrix} \epsilon_{xx} & \epsilon_{xy} \\ \epsilon_{xy} & \epsilon_{yy} \end{pmatrix} = \mathsf{R}(\varphi)^T \begin{pmatrix} \epsilon & \\ & -\nu_P \epsilon \end{pmatrix} \mathsf{R}(\varphi), \quad (1)$$

where $\nu_P \approx 0.16$ is the Poisson ratio of graphene. The angle φ corresponds to the uniaxial strain direction, and $\mathsf{R}(\varphi)$ is a 2×2 rotation matrix. Throughout this Letter, we take $\varphi = 0$, but we have verified that our conclusions do not depend on the choice of φ. The strain magnitude is determined by the dimensionless parameter ϵ, which in the devices prepared for STM study has values in the range $\epsilon = 0.1\%$–0.7% [27–29,35]. Under the combined effect of rotation and strain, the coordinates of the carbon atoms in the two graphene layers $\ell = \pm$ of TBG transform as $\mathbf{R}_{\ell,i} \to [\mathsf{R}(\ell\theta/2) - (\ell/2)\mathsf{S}]\mathbf{R}_{\ell,i} =: \mathsf{M}_\ell^T \mathbf{R}_{\ell,i}$ where θ is the twist angle. The coordinate transformation matrix M_ℓ^T is correct to first order in both θ and ϵ. Note that we only consider heterostrain, as it affects the electronic structure much more strongly than homostrain [36].

The continuum Hamiltonian in the presence of uniaxial heterostrain for the $\tau = +$ valley is given by

$$H_{\tau+} = \begin{pmatrix} D_+ & T(\mathbf{r}) \\ T(\mathbf{r})^\dagger & D_- \end{pmatrix}, \quad (2)$$

with D_ℓ the monolayer Dirac Hamiltonians and $T(\mathbf{r})$ the interlayer tunneling ($H_{\tau-}$ is then fully specified by time reversal). The Dirac Hamiltonians are given by

$$D_\ell = -\hbar v_F [\mathsf{M}_\ell(-i\nabla + \mathbf{A}_\ell) - \mathbf{K}] \cdot \boldsymbol{\sigma}, \quad (3)$$

where $\boldsymbol{\sigma} = (\sigma_x, \sigma_y)$ are Pauli matrices acting in sublattice space, and $\mathbf{K} = (4\pi/3a, 0)$, with a the graphene lattice constant, corresponds to the location of the $\tau = +$ valley. Strain shifts the locations of the Dirac points via a "vector potential" $\mathbf{A}_\ell = -(\ell/2)(\beta\sqrt{3}/2a)(\epsilon_{xx} - \epsilon_{yy}, -2\epsilon_{xy})$ [37,38], where $\beta \sim 3.14$ characterizes the dependence of the tight-binding hopping strength on the bond length.

The tunneling term $T(\mathbf{r})$ in Eq. (2) has the same form as in the original BM model, but we update the microscopic parameters to follow recent density functional theory calculations [39–41]. Specifically, we take differing intra and intersublattice interlayer tunneling amplitudes $w_{AA} = 83$ meV and $w_{AB} = 110$ meV. To account for nonzero strain ϵ, the moiré reciprocal lattice vectors are deformed to $\mathbf{g}_j = [\mathsf{M}_+^{-1} - \mathsf{M}_-^{-1}]\mathbf{G}_j$, where $\mathbf{G}_j$ are the reciprocal vectors of undeformed graphene.

As was shown in Ref. [34,36], uniaxial heterostrain has three important effects on the BM band spectrum: (i) while strain preserves $C_2\mathcal{T}$ symmetry and hence the stability of the two mini Dirac points, the threefold rotation symmetry is broken and the two Dirac points move away from the $K^\pm$ points toward the Γ point in the mini-BZ; (ii) the two Dirac points are no longer degenerate but are separated in energy by a few meV (thus creating small electron and hole pockets at the CNP); and (iii) the bandwidth of the "narrow" bands increases significantly—for ϵ as small as 0.6%, the bandwidth of the narrow bands is ∼50 meV. Below, we investigate the effect of strain on the interacting phase diagram of TBG.

Hartree-Fock at neutrality.—We model interacting TBG as the BM Hamiltonian plus Coulomb interactions:

$$H = \sum_{\mathbf{k}} f_{\mathbf{k}}^\dagger h(\mathbf{k}) f_{\mathbf{k}} + \frac{1}{2A} \sum_{\mathbf{q}} V_{\mathbf{q}} :\rho_{\mathbf{q}} \rho_{-\mathbf{q}}:, \quad (4)$$

where A is the area of the sample, and $f_{\mathbf{k},s,\tau,m}^\dagger$ creates an electron with momentum $\mathbf{k}$ and spin s in the BM band m in valley τ. The charge density operators are given by $\rho_{\mathbf{q}} = \sum_{\mathbf{k}} f_{\mathbf{k}}^\dagger \Lambda_{\mathbf{q}}(\mathbf{k}) f_{\mathbf{k}+\mathbf{q}}$, where the form factor matrices $[\Lambda_{\mathbf{q}}(\mathbf{k})]_{(\tau,m),(\tau',n)} = \delta_{\tau,\tau'} \langle u_{\tau,m,\mathbf{k}} | u_{\tau,n,\mathbf{k}+\mathbf{q}} \rangle$ are defined in terms of overlaps between the periodic part of the Bloch states of the BM Hamiltonian. The interaction is given by a gate screened Coulomb potential $V_{\mathbf{q}} = \int d\mathbf{r} e^{i\mathbf{q}\cdot\mathbf{r}} V(\mathbf{r}) = \tanh(d_s q)[2\varepsilon_0 \varepsilon_r q]^{-1}$. We work with a gate distance of $d_s = 25$ nm, and we let the dielectric constant ε_r vary between 6 and 12. In Eq. (4), we also project into a subspace where most or all of the remote BM valence (conduction) bands are completely filled (empty), and m, n run over only those bands whose filling is not fixed. The single-particle Hamiltonian $h(\mathbf{k})$ contains the BM band energies, an HF contribution from the remote filled bands, and a subtraction term [21,30]. For more details on the definition of $h(\mathbf{k})$, see Ref. [32].

Without strain, Ref. [22] found that the ground state of H at $\nu = -2, 0, 2$ has a charge gap and spontaneously breaks both the valley charge symmetry $e^{i\alpha\tau_z}$ and the time-reversal symmetry $\mathcal{T} = \tau_x K$, where K denotes complex conjugation. However, the product $\mathcal{T}' = e^{i\pi\tau_z/2}\mathcal{T}$ is preserved. Because $\mathcal{T}' = \tau_y K$ is a (spinless) Kramers time reversal, the insulating ground state was dubbed the Kramers intervalley-coherent (K-IVC) state [22].

Figure 1 shows the HF phase diagram at the CNP as a function of twist angle and strain magnitude for both $\varepsilon_r = 6$ and $\varepsilon_r = 12$. (Note that, throughout this work, we allow HF to break all symmetries except for the translation symmetry.) Two phases are clearly visible. The region in Fig. 1 with nonzero charge gap has K-IVC order. The gapless region, on the other hand, corresponds to a semimetal (SM) without spontaneous symmetry breaking. The HF band structure of the SM has two Dirac cones close to the Γ point and is therefore similar to the band structure of the strained BM Hamiltonian (for more details, see [42]). The transition from the K-IVC state to the SM in Fig. 1 occurs at strain values $\epsilon \sim 0.4\%$–0.6% with $\varepsilon_r = 6$ and at $\epsilon \sim 0.1\%$–0.2% with $\varepsilon_r = 12$. These critical values lie exactly in the range of strain values observed in STM devices [27–29,35], from which we conclude that strain plays an important role in TBG. From Fig. 1, we also see that the K-IVC state is more

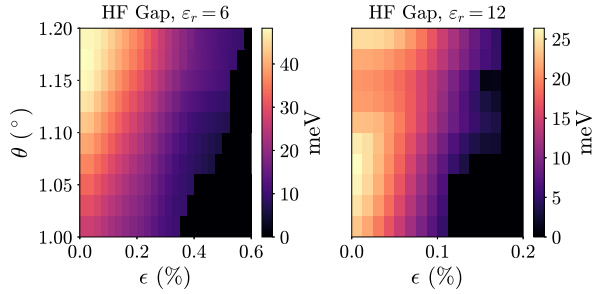

FIG. 1. Particle-hole gap in the SCHF band spectrum at the CNP as a function of both twist angle θ and strain ϵ, for $\varepsilon_r = 6$ (left) and $\varepsilon_r = 12$ (right). The results were obtained on a 18×18 momentum grid, keeping six bands per spin and valley. The gapped regions have K-IVC order; the gapless regions correspond to a symmetric SM.

robust at larger θ. Because at $\epsilon = 0$ the energy difference between the K-IVC state and the SM depends only weakly on θ [22], we attribute this feature to the fact that the active bands are less affected by strain at larger θ (in particular, the Dirac points remain further away from Γ, and the change in bandwidth is smaller).

In Fig. 2(a), we plot the K-IVC order parameter as a function of ϵ. The order parameter is defined as $|\Delta_{\text{K-IVC}}| \coloneqq (1/N)\sum_{\mathbf{k}} \|\mathsf{P}_{\text{IVC}}(\mathbf{k})\|$, where N is the number of $\mathbf{k}$ values and P_{IVC} is the intervalley ($\tau \neq \tau'$) part of the K-IVC correlation matrix $[\mathsf{P}(\mathbf{k})]_{(s,\tau,m),(s',\tau',n)} = \langle f^{\dagger}_{\mathbf{k},s',\tau',n} f_{\mathbf{k},s,\tau,m}\rangle$. We see that the transition occurs at $\epsilon_* \sim 0.19\%$ if we keep $N_b = 6$ BM bands per spin and valley. By increasing N_b, ϵ_* shifts to slightly smaller values and converges for $N_b = 12$. Figure 2(a) shows a discontinuity in $|\Delta_{\text{K-IVC}}|$, implying that the transition is first order. However, we also find that close to the transition, $|\Delta_{\text{K-IVC}}|$ decreases by a factor of 20 (using $N_b = 12$) compared to its value at $\epsilon = 0$. We therefore cannot exclude that the weakly first-order behavior is an artifact of HF.

Figure 2(b) shows the density of states (DOS) obtained in SCHF for different ϵ, interpolating between the K-IVC insulator and the SM. The dominant feature for both the K-IVC and SM DOS is a pair of broad peaks separated by ~50 meV. In the K-IVC phase, there is a finite window around the Fermi energy where the DOS is zero, which decreases with ϵ and vanishes at the transition. This is a subtle feature, however, making it hard to sharply distinguish the SM from the K-IVC. A finer probe for the properties of the SM is the (layer-resolved) local DOS (LDOS) [42]. In Figs. 3(a),(b), we plot the LDOS of the SM at energies $E/W = -0.11$ and $E/W = 0.15$, where W is the HF bandwidth. The LDOS at the AA regions shows strong C_{3z} breaking. This strong C_{3z} breaking results from interactions, as it does not show up in the LDOS of the BM ground state at the same energy ratios $E/W_0 = -0.11$ and $E/W_0 = 0.15$, where W_0 is the BM bandwidth [see Figs. 3(c),(d) and [42]]. These properties of the HF LDOS agree with STM experiments [27,28,43]. In particular, Ref. [43] observed strong C_{3z} breaking at the CNP but not at $\nu = 4$. We calculated the LDOS at this filling, where the active bands are fully filled, and indeed found almost no reconstruction of the BM LDOS by interactions and, as a result, no strong C_{3z} breaking.

Finally, strain can be invoked to explain the degeneracies of the Landau fan near the CNP [33,34] of the SM. At low densities, quantum oscillations are governed by cyclotron orbits around the mini Dirac points, with two Dirac points for each of the four isospins. When mirror symmetry (C_{2x}) ensures that the two Dirac points are equivalent, the resulting Landau fan will have the eightfold degeneracy $\nu_\phi = \pm 4, \pm 12, \pm 20, \ldots$, which is observed, for example, far from the magic angle. However, mirror symmetry is broken by strain: for example, at $\epsilon = 0.22\%$ and $\varepsilon_r = 10$,

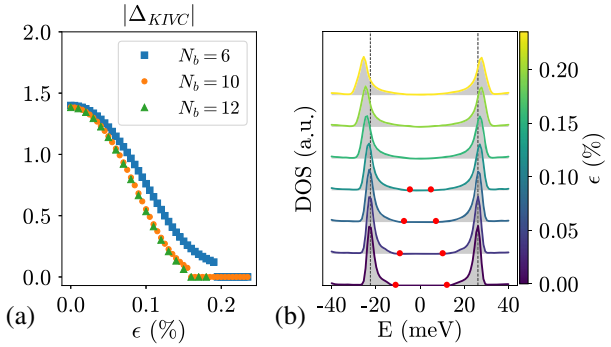

FIG. 2. (a) K-IVC order parameter $|\Delta_{\text{K-IVC}}| \coloneqq (1/N)\sum_{\mathbf{k}} \|\mathsf{P}_{\text{IVC}}(\mathbf{k})\|$ at charge neutrality as a function of ϵ, obtained with SCHF using $\theta = 1.05°$, $\varepsilon_r = 10$, and $N_b = 6$, 10, or 12 bands per spin and valley. The calculations were done on a 24×24 momentum grid. (b) DOS of the SCHF band spectrum on a 36×36 momentum grid using $\theta = 1.05°$, $\varepsilon_r = 10$, and $N_b = 6$. The edges of the K-IVC gap are indicated with red dots.

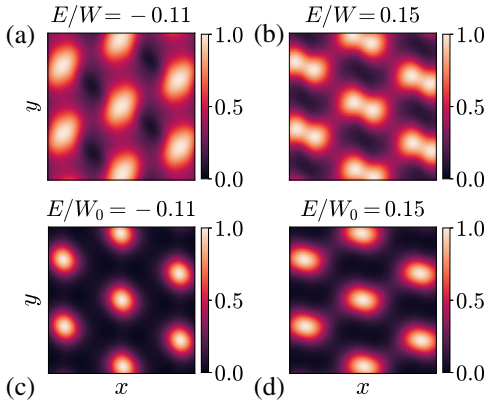

FIG. 3. Normalized LDOS for $\theta = 1.05°$ and $\epsilon = 0.22\%$. (a), (b) LDOS of the self-consistent SM (for $\varepsilon_r = 10$) at $E/W = -0.11$ and $E/W = 0.15$, where $W \sim 65$ meV is the HF bandwidth. (c),(d) LDOS of the BM ground state at $E/W_0 = -0.11$ and $E/W_0 = 0.15$, where $W_0 \sim 17$ meV is the BM bandwidth.

we find that the two Dirac points in the same valley are separated in energy by $\Delta_D \sim 10$ meV. For generic B, this halves the degeneracy, $\nu_\phi = 0, \pm 4, \pm 8, \pm 12, \ldots$, as observed in most magic-angle experiments [2,3]. When $|\nu| \gtrsim 0.25$, the cyclotron orbits of the two Dirac points merge and form one connected orbit with a 2π-Berry phase. Because the resulting Landau fan $\nu_\phi = \pm 4, \pm 8, \pm 12, \ldots$ has the same fourfold degeneracy as the Δ_D-split Dirac points, the conclusion is the same. However, we note that some devices show a crossover from a low-B eightfold degeneracy to a high-B fourfold degeneracy (for example, at $B \sim 1$ T in Ref. [44]). It may be that in devices where the strain configuration happens to produce a small Δ_D, the mirror breaking manifests in the terms that are linear in B.

DMRG at $\nu = -2$.—While SCHF is a mean field approach, we may further confirm the existence of a strain-induced transition using unbiased DMRG calculations. In Ref. [22], it was argued that, in the absence of strain, the ground state of the interacting Hamiltonian H at fillings $\nu = \pm 2$ is a spin-polarized version of the K-IVC state at neutrality. This claim was further substantiated by Refs. [45–47]. Following the methods developed in Refs. [31,32,48], here we use infinite DMRG to study H compactified onto a infinitely long cylinder of circumference L_y moiré cells. SCHF finds that the ground state is perfectly spin polarized for $\epsilon \lesssim 0.2\%$, so we accelerate our DMRG calculations by assuming full spin polarization of the narrow bands at $\nu = -2$ while keeping both valleys [42]. Projecting into the narrow bands, our computational basis for the four remaining active bands consists of hybrid Wannier orbitals that are localized in the x direction but have the well-defined momentum $k_y = 2\pi n/L_y$.

The ground state of the unstrained model at $\nu = -2$ is expected to have K-IVC order and thus to spontaneously break the $U(1)$ valley symmetry. The Hohenberg-Mermin-Wagner theorem, however, forbids such continuous symmetry breaking on the quasi-1D cylinder geometry used by DMRG [49,50]. Instead, the K-IVC phase will manifest as algebraic long-range order [51] $C_K(x) \coloneqq \langle \Delta_K^+(x)\Delta_K^-(0)\rangle \sim x^{-\eta(L_y)}$, where $\Delta_K^\pm(x)$ are operators at position x that have valley charge ± 2 and satisfy $\mathcal{T}'^{-1} O_K^\pm(x) \mathcal{T}' = O_K^\mp(x)$ [42]. The exponent $\eta(L_y)$ depends on the circumference and satisfies $\eta(\infty) = 0$. An additional complication for identifying the K-IVC phase using DMRG is that at any finite DMRG bond dimension χ (i.e., numerical accuracy), the ground state has exponentially decaying correlations. This complication can be overcome by using "finite entanglement scaling" [52–54] to characterize algebraic order via a scaling collapse as $\chi \to \infty$. Denoting the finite-χ induced correlation length as ξ_K [Fig. 4(c)], the K-IVC correlator can be written as a general function $C_K(x, \xi_K)$. In the K-IVC phase, we expect this function to satisfy the scaling relation $C_K(x, \xi_K) = \xi_K^{-\eta} C_K(x/\xi_K, 1)$, which allows us to perform a scaling collapse of the data obtained at different χ. In Fig. 4(a), we find an excellent data collapse for χ

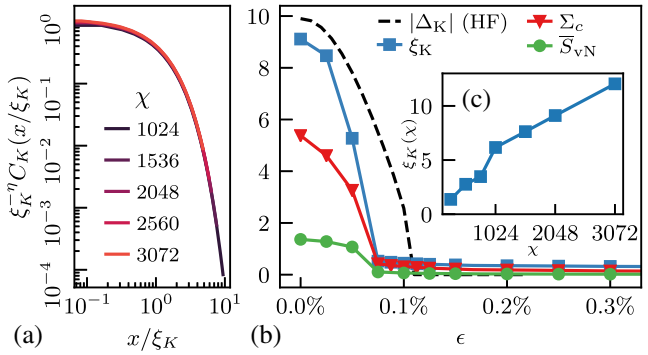

FIG. 4. DMRG results at $\nu = -2$ (spin polarized) at $\theta = 1.05°$ and $\varepsilon_r = 10$. (a) Scaling collapse of the K-IVC correlator $C_K(x, \xi_K)$ at $\epsilon = 0$. (b) Transition from K-IVC to SM with strain. K-IVC correlation length ξ_K, average entropy $\bar{S}_{vN}$, the DMRG K-IVC correlator $\Sigma_C = 10 \sum_x C_K(x)$ (scaled for visibility), and the HF K-IVC correlator $|\Delta_{\text{K–IVC}}|$ as a function of ϵ. (c) Scaling of ξ_K with bond dimension at $\epsilon = 0$. DMRG parameters: $L_y = 6$, $\Phi_y = 0$, $\chi \approx 2048$ for (b), and the Hamiltonian, Eq. (4), is represented to accuracy better than 0.1 meV. All quantities are defined in the text.

ranging between 1024 and 3072, from which we conclude that DMRG indeed finds a K-IVC ground state. Note that we find a very small exponent $\eta(6) \sim 0.06$ [42], so there is no regime of algebraic decay clearly visible in Fig. 4(a).

Figure 4(b) shows the effect of adding strain. Both the correlation length ξ_K and summed correlator $\Sigma_C \coloneqq \sum_x C_K(x)$ measure the amount of K-IVC correlations in the ground state. They are both order 1 for small strain and decrease monotonically with ϵ. For $\epsilon \gtrsim 0.07\%$, however, ξ_K and Σ_C plateau at a small value, indicating that the algebraic K-IVC order is destroyed. For strain values larger than $\sim$0.07%, we find no evidence for symmetry breaking in the DMRG ground state. In particular, we have verified that DMRG does not double the unit cell, which excludes the stripe phase discussed previously for single-valley models [31,32]. The absence of symmetry breaking in DMRG is consistent with HF, where we find a symmetric SM at large ϵ [42]. Figure 4(b) plots the SCHF order parameter $|\Delta_{\text{K-IVC}}|$, which shows a transition from the K-IVC state to the SM at a strain value $\epsilon \sim 0.1\%$, close to where the algebraic K-IVC order disappears in DMRG. While the behavior of the DMRG correlation length is consistent with a first-order transition, much larger bond dimensions—and cylinder circumferences—would be needed to decide this issue. To confirm that the large strain phase found with DMRG is the same SM obtained in SCHF, we compute the averaged single particle entropy $\bar{S}_{\text{vN}} \coloneqq -(1/N) \sum_{\mathbf{k}} \text{tr}[\mathsf{P}(\mathbf{k}) \ln \mathsf{P}(\mathbf{k})]$. This quantity is zero if the DMRG ground state is a Slater determinant. Figure 4(b) shows that $\bar{S}_{\text{vN}}$ is negligibly small at $\epsilon \gtrsim 0.07\%$ (at smaller ϵ, the Hohenberg-Mermin-Wagner theorem implies the K-IVC state cannot be a symmetry breaking Slater determinant in DMRG, so $\bar{S}_{\text{vN}}$ is order unity). It thus follows that

(i) SCHF and DMRG agree closely for all strain and are essentially identical at large ϵ, and (ii) the transition in DMRG is indeed from the K-IVC state to the SM.

Discussion.—The results presented in this Letter show that strain is likely responsible for the semimetallic behavior and strong C_{3z} breaking observed at the CNP of most TBG devices (for related discussions of the CNP physics, see Refs. [55,56]). C_{3z} breaking has also been observed in TBG near $\nu = -2$ [4] and was discussed in various theoretical contexts in Refs. [57–60]. From our DMRG and SCHF results, we found that TBG couples strongly to strain both at $\nu = 0$ and $\nu = -2$. Two important questions that follow from this are (i) whether the strong coupling to strain persists to $\nu = -2 - \delta$ with $\delta \sim 0.1$–0.9 (where nematicity was observed in experiment [4]), and (ii) whether strain is important for superconductivity. Our findings also invigorate the question about the origin of the insulating behavior consistently observed at $\nu = -2$, as we find that within the model studied here, strain drives the K-IVC–SM transition at roughly the same ϵ for both $\nu = 0$ and $\nu = -2$. One possibility is that band structure effects we have neglected, such as lattice relaxation [39,41] or nonlocal interlayer tunneling [41,61], stabilize the insulators at $\nu = \pm 2$ at larger strain values.

We want to thank Eslam Khalaf, Shubhayu Chatterjee, and Ashvin Vishwanath for helpful discussions. N. B. would like to thank Glenn Wagner and Yves Kwan for useful feedback on an earlier version of this manuscript. N. B. was supported by a fellowship of the Research Foundation Flanders (FWO) under Contract no. 1287321N. D. E. P. was funded by the Gordon and Betty Moore Foundation's EPiQS Initiative Grant No. GBMF8683. M. P. Z. was supported by the Director, Office of Science, Office of Basic Energy Sciences, Materials Sciences and Engineering Division of the U.S. Department of Energy under Contract no. DE-AC02-05-CH11231 (van der Waals heterostructures program, KCWF16). J. H. was funded by the U.S. Department of Energy, Office of Science, Office of Basic Energy Sciences, Materials Sciences and Engineering Division under Contract no. DE-AC02-05- CH11231 through the Scientific Discovery through Advanced Computing (SciDAC) program (KC23DAC Topological and Correlated Matter via Tensor Networks and Quantum Monte Carlo). This research used the Savio computational cluster resource provided by the Berkeley Research Computing program at the University of California, Berkeley (supported by the UC Berkeley Chancellor, Vice Chancellor for Research, and Chief Information Officer).

[1] Y. Cao, V. Fatemi, A. Demir, S. Fang, S. L. Tomarken, J. Y. Luo, J. D. Sanchez-Yamagishi, K. Watanabe, T. Taniguchi, E. Kaxiras *et al.*, Correlated insulator behaviour at half-filling in magic-angle graphene superlattices, Nature (London) **556**, 80 (2018).

[2] Y. Cao, V. Fatemi, S. Fang, K. Watanabe, T. Taniguchi, E. Kaxiras, and P. Jarillo-Herrero, Unconventional superconductivity in magic-angle graphene superlattices, Nature (London) **556**, 43 (2018).

[3] M. Yankowitz, S. Chen, H. Polshyn, Y. Zhang, K. Watanabe, T. Taniguchi, D. Graf, A. F. Young, and C. R. Dean, Tuning superconductivity in twisted bilayer graphene, Science, **363**, 1059 (2019).

[4] Y. Cao, D. Rodan-Legrain, J. M. Park, F. N. Yuan, K. Watanabe, T. Taniguchi, R. M. Fernandes, L. Fu, and P. Jarillo-Herrero, Nematicity and competing orders in superconducting magic-angle graphene, arXiv:2004.04148.

[5] X. Liu, Z. Wang, K. Watanabe, T. Taniguchi, O. Vafek, and J. I. A. Li, Tuning electron correlation in magic-angle twisted bilayer graphene using Coulomb screening, arXiv:2003.11072.

[6] J. M. Park, Y. Cao, K. Watanabe, T. Taniguchi, and P. Jarillo-Herrero, Flavour Hund's coupling, correlated chern gaps, and diffusivity in Moiré flat bands, arXiv:2008.12296.

[7] A. L. Sharpe, E. J. Fox, A. W. Barnard, J. Finney, K. Watanabe, T. Taniguchi, M. A. Kastner, and D. Goldhaber-Gordon, Emergent ferromagnetism near three-quarters filling in twisted bilayer graphene, Science **365**, 605 (2019).

[8] M. Serlin, C. L. Tschirhart, H. Polshyn, Y. Zhang, J. Zhu, K. Watanabe, T. Taniguchi, L. Balents, and A. F. Young, Intrinsic quantized anomalous Hall effect in a moiré heterostructure, Science **367**, 900 (2020).

[9] X. Lu, P. Stepanov, W. Yang, M. Xie, M. A. Aamir, I. Das, C. Urgell, K. Watanabe, T. Taniguchi, G. Zhang, A. Bachtold, A. H. MacDonald, and D. K. Efetov, Superconductors, orbital magnets, and correlated states in magic angle bilayer graphene, Nature (London) **574**, 653 (2019).

[10] P. Stepanov, I. Das, X. Lu, A. Fahimniya, K. Watanabe, T. Taniguchi, F. H. Koppens, J. Lischner, L. Levitov, and D. K. Efetov, The interplay of insulating and superconducting orders in magic-angle graphene bilayers, arXiv:1911.09198.

[11] S. Wu, Z. Zhang, K. Watanabe, T. Taniguchi, and E. Y. Andrei, Chern insulators and topological flat-bands in magic-angle twisted bilayer graphene, arXiv:2007.03735.

[12] B. Hunt, J. D. Sanchez-Yamagishi, A. F. Young, M. Yankowitz, B. J. LeRoy, K. Watanabe, T. Taniguchi, P. Moon, M. Koshino, P. Jarillo- Herrero, and R. C. Ashoori, Massive Dirac fermions and Hofstadter butterfly in a van der Waals heterostructure, Science **340**, 1427 (2013).

[13] F. Amet, J. R. Williams, K. Watanabe, T. Taniguchi, and D. Goldhaber-Gordon, Insulating Behavior at the Neutrality Point in Single-Layer Graphene, Phys. Rev. Lett. **110**, 216601 (2013).

[14] A. A. Zibrov, E. M. Spanton, H. Zhou, C. Kometter, T. Taniguchi, K. Watanabe, and A. F. Young, Even-denominator fractional quantum Hall states at an isospin transition in monolayer graphene, Nat. Phys. **14**, 930 (2018).

[15] J. Jung, A. M. DaSilva, A. H. MacDonald, and S. Adam, Origin of band gaps in graphene on hexagonal boron nitride, Nat. Commun. **6**, 6308 (2015).

[16] M. Yankowitz, J. Jung, E. Laksono, N. Leconte, B. L. Chittari, K. Watanabe, T. Taniguchi, S. Adam, D. Graf, and

C. R. Dean, Dynamic band-structure tuning of graphene moiré superlattices with pressure, Nature (London) **557**, 404 (2018).
[17] H. Kim, N. Leconte, B. L. Chittari, K. Watanabe, T. Taniguchi, A. H. MacDonald, J. Jung, and S. Jung, Accurate gap determination in monolayer and bilayer graphene/h-BN Moiré superlattices, Nano Lett. **18**, 7732 (2018).
[18] R. Bistritzer and A. H. MacDonald, Moiré bands in twisted double-layer graphene, Proc. Natl. Acad. Sci. U.S.A. **108**, 12233 (2011).
[19] E. S. Morell, J. D. Correa, P. Vargas, M. Pacheco, and Z. Barticevic, Flat bands in slightly twisted bilayer graphene: Tight-binding calculations, Phys. Rev. B **82**, 121407(R) (2010).
[20] J. M. B. Lopes dos Santos, N. M. R. Peres, and A. H. Castro Neto, Continuum model of the twisted graphene bilayer, Phys. Rev. B **86**, 155449 (2012).
[21] M. Xie and A. H. MacDonald, Nature of the Correlated Insulator States in Twisted Bilayer Graphene, Phys. Rev. Lett. **124**, 097601 (2020).
[22] N. Bultinck, E. Khalaf, S. Liu, S. Chatterjee, A. Vishwanath, and M. P. Zaletel, Ground State and Hidden Symmetry of Magic-Angle Graphene at Even Integer Filling, Phys. Rev. X **10**, 031034 (2020).
[23] A. Uri, S. Grover, Y. Cao, J. A. Crosse, K. Bagani, D. Rodan-Legrain, Y. Myasoedov, K. Watanabe, T. Taniguchi, P. Moon, M. Koshino, P. Jarillo-Herrero, and E. Zeldov, Mapping the twist-angle disorder and landau levels in magic-angle graphene, Nature (London) **581**, 47 (2020).
[24] U. Zondiner, A. Rozen, D. Rodan-Legrain, Y. Cao, R. Queiroz, T. Taniguchi, K. Watanabe, Y. Oreg, F. von Oppen, A. Stern, E. Berg, P. Jarillo-Herrero, and S. Ilani, Cascade of phase transitions and dirac revivals in magic-angle graphene, Nature (London) **582**, 203 (2020).
[25] J. H. Wilson, Y. Fu, S. D. Sarma, and J. H. Pixley, Disorder in twisted bilayer graphene, Phys. Rev. Research **2**, 023325 (2020).
[26] B. Padhi, A. Tiwari, T. Neupert, and S. Ryu, Transport across twist angle domains in Moiré graphene, Phys. Rev. Research **2**, 033458 (2020).
[27] A. Kerelsky, L. J. McGilly, D. M. Kennes, L. Xian, M. Yankowitz, S. Chen, K. Watanabe, T. Taniguchi, J. Hone, C. Dean, A. Rubio, and A. N. Pasupathy, Maximized electron interactions at the magic angle in twisted bilayer graphene, Nature (London) **572**, 95 (2019).
[28] Y. Choi, J. Kemmer, Y. Peng, A. Thomson, H. Arora, R. Polski, Y. Zhang, H. Ren, J. Alicea, G. Refael, F. von Oppen, K. Watanabe, T. Taniguchi, and S. Nadj-Perge, Electronic correlations in twisted bilayer graphene near the magic angle, Nat. Phys. **15**, 1174 (2019).
[29] Y. Xie, B. Lian, B. Jäck, X. Liu, C.-L. Chiu, K. Watanabe, T. Taniguchi, B. A. Bernevig, and A. Yazdani, Spectroscopic signatures of many-body correlations in magic-angle twisted bilayer graphene, Nature (London) **572**, 101 (2019).
[30] S. Liu, E. Khalaf, J. Y. Lee, and A. Vishwanath, Nematic topological semimetal and insulator in magic angle bilayer graphene at charge neutrality, Phys. Rev. Research **3**, 013033 (2021).
[31] J. Kang and O. Vafek, Non-abelian dirac node braiding and near-degeneracy of correlated phases at odd integer filling in magic-angle twisted bilayer graphene, Phys. Rev. B **102**, 035161 (2020).
[32] T. Soejima, D. E. Parker, N. Bultinck, J. Hauschild, and M. P. Zaletel, Efficient simulation of moiré materials using the density matrix renormalization group, Phys. Rev. B **102**, 205111 (2020).
[33] Y.-H. Zhang, H. C. Po, and T. Senthil, Landau level degeneracy in twisted bilayer graphene: Role of symmetry breaking, Phys. Rev. B **100**, 125104 (2019).
[34] Z. Bi, N. F. Q. Yuan, and L. Fu, Designing flat bands by strain, Phys. Rev. B **100**, 035448 (2019).
[35] Y. Choi, H. Kim, Y. Peng, A. Thomson, C. Lewandowski, R. Polski, Y. Zhang, H. Singh Arora, K. Watanabe, T. Taniguchi, J. Alicea, and S. Nadj-Perge, Tracing out correlated Chern insulators in magic angle twisted bilayer graphene, arXiv:2008.11746.
[36] L. Huder, A. Artaud, T. Le Quang, G. T. de Laissardière, A. G. M. Jansen, G. Lapertot, C. Chapelier, and V. T. Renard, Electronic Spectrum of Twisted Graphene Layers Under Heterostrain, Phys. Rev. Lett. **120**, 156405 (2018).
[37] H. Suzuura and T. Ando, Phonons and electron-phonon scattering in carbon nanotubes, Phys. Rev. B **65**, 235412 (2002).
[38] K.-I. Sasaki and R. Saito, Pseudospin and deformation-induced gauge field in graphene, Prog. Theor. Phys. Suppl. **176**, 253 (2008).
[39] N. N. T. Nam and M. Koshino, Lattice relaxation and energy band modulation in twisted bilayer graphene, Phys. Rev. B **96**, 075311 (2017).
[40] M. Koshino, N. F. Q. Yuan, T. Koretsune, M. Ochi, K. Kuroki, and L. Fu, Maximally Localized Wannier Orbitals and the Extended Hubbard Model for Twisted Bilayer Graphene, Phys. Rev. X **8**, 031087 (2018).
[41] S. Carr, S. Fang, Z. Zhu, and E. Kaxiras, Exact continuum model for low-energy electronic states of twisted bilayer graphene, Phys. Rev. Research **1**, 013001 (2019).
[42] See Supplemental Material at http://link.aps.org/supplemental/10.1103/PhysRevLett.127.027601 for a discussion of the connection between the BM ground state and the self-consistent SM at charge neutrality, for HF results at $\nu = -2$, and for additional details of the DMRG simulations.
[43] Y. Jiang, X. Lai, K. Watanabe, T. Taniguchi, K. Haule, J. Mao, and E. Y. Andrei, Charge order and broken rotational symmetry in magic-angle twisted bilayer graphene, Nature (London) **573**, 91 (2019).
[44] Y. Saito, J. Ge, K. Watanabe, T. Taniguchi, and A. F. Young, Independent superconductors and correlated insulators in twisted bilayer graphene, Nat. Phys. **16**, 926 (2020).
[45] J. Kang and O. Vafek, Strong Coupling Phases of Partially Filled Twisted Bilayer Graphene Narrow Bands, Phys. Rev. Lett. **122**, 246401 (2019).
[46] Y. Zhang, K. Jiang, Z. Wang, and F. Zhang, Correlated insulating phases of twisted bilayer graphene at commensurate filling fractions: A Hartree-Fock study, Phys. Rev. B **102**, 035136 (2020).
[47] B. Lian, Z.-D. Song, N. Regnault, D. K. Efetov, A. Yazdani, and B. A. Bernevig, TBG IV: Exact insulator ground states and phase diagram of twisted bilayer graphene, Phys. Rev. B **103**, 205414 (2021).

[48] J. Hauschild and F. Pollmann, Efficient numerical simulations with tensor networks: Tensor network python (TeNPy), SciPost Phys. Lect. Notes, 5 (2018), code available from https://github.com/tenpy/tenpy, arXiv: 1805.00055.

[49] P. C. Hohenberg, Existence of long-range order in one and two dimensions, Phys. Rev. **158**, 383 (1967).

[50] N. D. Mermin and H. Wagner, Absence of Ferromagnetism or Antiferromagnetism in One- or Two-Dimensional Isotropic Heisenberg Models, Phys. Rev. Lett. **17**, 1133 (1966).

[51] S. Chatterjee, M. Ippoliti, and M. P. Zaletel, Skyrmion Superconductivity: DMRG evidence for a topological route to superconductivity, arXiv:2010.01144.

[52] F. Pollmann, S. Mukerjee, A. M. Turner, and J. E. Moore, Theory of Finite-Entanglement Scaling at One-Dimensional Quantum Critical Points, Phys. Rev. Lett. **102**, 255701 (2009).

[53] L. Tagliacozzo, T. R. de Oliveira, S. Iblisdir, and J. I. Latorre, Scaling of entanglement support for matrix product states, Phys. Rev. B **78**, 024410 (2008).

[54] J. A. Kjäll, M. P. Zaletel, R. S. K. Mong, J. H. Bardarson, and F. Pollmann, Phase diagram of the anisotropic spin-2 xxz model: Infinite-system density matrix renormalization group study, Phys. Rev. B **87**, 235106 (2013).

[55] E. Brillaux, D. Carpentier, A. A. Fedorenko, and L. Savary, Nematic insulator at charge neutrality in twisted bilayer graphene, arXiv:2008.05041.

[56] H. Ochoa, Strain-induced excitonic instability in twisted bilayer graphene, Phys. Rev. B **102**, 201107 (2020).

[57] R. M. Fernandes and J. W. F. Venderbos, Nematicity with a twist: Rotational symmetry breaking in a Moiré superlattice, Sci. Adv. **6**, https://doi.org/10.1126/sciadv.aba8834 (2020).

[58] Y. Wang, J. Kang, and R. M. Fernandes, Topological and nematic superconductivity mediated by ferro-SU(4) fluctuations in twisted bilayer graphene, Phys. Rev. B **103**, 024506 (2021).

[59] D. V. Chichinadze, L. Classen, and A. V. Chubukov, Nematic superconductivity in twisted bilayer graphene, Phys. Rev. B **101**, 224513 (2020).

[60] V. Kozii, H. Isobe, J. W. F. Venderbos, and L. Fu, Nematic superconductivity stabilized by density wave fluctuations: Possible application to twisted bilayer graphene, Phys. Rev. B **99**, 144507 (2019).

[61] M. Xie and A. H. MacDonald, Weak-field Hall resistivity and spin/valley flavor symmetry breaking in MAtBG, arXiv:2010.07928.